

Simulation and Experimental Analysis of Double Rotating Shoulder Friction Stir Welding

Jianhui Wu¹ · Tao Sun¹ · Zhenkui Liang¹ ·
Yongqi Yang¹ · Xiaomei Feng¹ · Yifu Shen¹ 

Received: 31 January 2024 / Accepted: 10 May 2024 / Published online: 29 May 2024
© The Indian Institute of Metals - IIM 2024

Abstract In this work, a new Double Rotating Shoulder (DRS) tool is designed to create a preheating effect and promote material flow in the shoulder-affected area during friction stir welding (FSW). A comparative study of the temperature field, strain field and material flow of AA 6061 aluminium alloy during FSW using a DRS tool and a conventional tool was carried out using numerical simulation. The model was verified according to the actual temperature field in both cases. Further, the macroscopic morphology and mechanical properties of both joints were investigated. The results showed that the simulated temperature field during FSW using a DRS tool has a good correlation with the actual temperature field. The DRS tool does lead to different macroscopic profiles but has almost no impact on mechanical properties.

Keywords Double rotating shoulder · Macroscopic morphology · Temperature field simulation · Strain field simulation · Material flow simulation

1 Introduction

Friction stir welding is a novel solid joining technology [1]. Compared to traditional welding of aluminium alloys, it does not require any shielding gas or filler material. Additionally, it has the advantage of being pollution-free, with no arc light, noise, or radiation [2]. The heat input in the friction

stir welding process primarily results from the mechanical friction between the stirring head (comprising the shoulder and the pin) and the workpiece to be welded. Additionally, plastic deformation of the material contributes to the heat generation [3]. In recent years, With the further development of friction stir welding technology, a number of variants have been derived from conventional friction stir welding devices, which incorporate the addition of a cooling medium, the addition of a second device (laser, arc, induction, etc.), and innovative tool designs (dual rotating-axis friction stir welding, stationary-axis shoulder friction stir welding, etc.).

Researchers in order to solve the FSW in the welding process, due to the heat input of the stirring head is too large grain size problem, added cooling medium to reduce the thermal cycle of the welding process. Cao et al. [4] studied the super duplex stainless steel underwater stirring friction; underwater FSW and air FSW comparison results showing that due to the flow of water, underwater FSW can significantly weaken the welding thermal cycle, joint's organisation is more uniform and the grain size is finer, and the mechanical properties are enhanced. Cao et al. [5] used a flowing low-temperature medium for stirring friction processing of duplex stainless steel, and the results showed that the joints obtain uniform ultrafine crystalline duplex organisation and fine grains, and the yield strength significantly increases and maintains a high elongation. Due to the problem of defects in the weld due to insufficient heat generation and plastic flow in conventional friction stir welding of high melting point materials, researchers have proposed a second heat source. Fei et al. [6] used a laser-assisted FSW process to weld 3 mm thick Q235 steel and 6061-T6 aluminium alloy, and investigated the effect of the preset hole offset distance on the properties of the welded joints, and found out that the preset hole offset has a large effect on the thickness and type of IMCS at the interface. Yaduwanshi

✉ Yifu Shen
shenyifu0501@gmail.com

¹ College of Materials Science and Technology, Nanjing University of Aeronautics and Astronautics (NUAA), 29 Jiangjun Road, Nanjing 210016, People's Republic of China

et al. [7] carried out simulation and experimental validation of plasma-assisted friction stir welding (P-FSW) process and showed that the maximum temperature on the copper side is 316–378 K higher than that on the aluminium side and the preheating reduces the difference in yield stresses to 10 Mpa, which is conducive to the welding of different materials in this process. Kaushik et al. [8] used induction heating FSW process to weld 3 mm thick industrially pure aluminium and mild steel and investigated the weld performance under this process and found that induction preheating of the steel plate increases the ductility of the welded joint by about 34%. Although it is possible to improve material flow, plasticizing materials and joint properties during FSW by means of a cooling medium and a second heat source, it increases the preparation work for welding, complicates the FSW tooling and increases the economic costs. In contrast, innovative tool designs have the potential for greater application demand.

The design of the innovative tool is mainly centred around the shaft shoulder, which can be classified into dual rotating shaft friction stir welding device and static shaft shoulder friction stir welding device according to the working condition of the shoulder. Among them, the static-shoulder friction stir welding idea was initially proposed by Arthur of NASA MSFC and proved by Talia of Wichita State University in 2002 [9, 10]. Li and Liu [11, 12] welded 2219-t6 aluminium alloy by using an external non-rotating shoulder-assisted friction stir welding (nsa-fsw), and studied the effects of the tool rotational speed and research speed on the organisation and mechanical properties of the aluminium alloy; the results showed that good joints can be obtained in the range of 600–900 rpm, where the maximum values of tensile strength and elongation is obtained when the tool is at 800 rpm. Defect-free joints can be obtained at welding speeds in the range of 50–300 mm/min. Barbini et al. [13] studied the differences between AA2022-T3 and AA7050-T7651 aluminium alloys under two processes, stir friction welding and static shoulder stir friction welding (ssfsw), and the results showed that the joint weld area and interfacial diffusion are reduced and the tensile strength and elongation of joints decrease in ssfsw. Sinhmar et al. [14] developed a new type of static shoulder FSW (SSFSW) and the results showed that the heat generation from the fixed shoulder is smaller than that of conventional FSW and the mechanical properties of the joints are improved. Saravana Sundar et al. [15] used an independently designed static shoulder friction welding device to weld AA6061 aluminium alloy and compared it with conventional FSW and underwater FSW and the results showed that SSFSW possesses the smallest grain size. Literature survey summarizes that, although static shoulder stir friction welding can effectively improve the welded joint properties, it increases the equipment load and tooling requirements during the welding process because the shoulder is static. However, these problems can be

avoided when we design the stationary shoulder as a rotating shoulder.

However, there is still very little research on tandem twin rotating axis stir friction welding compared to the research on stationary axis shoulder stir friction welding. The concept of dual rotating axis stir friction welding was initially proposed by Thomas [16], followed by a tandem dual-axis stir friction welding technique published [17–20]. Kumari et al. [21] welded A1100 aluminium alloy using front to back parallel double stirrer head and found that the hardness distribution of the weld at 1800 rpm is higher in double stirrer head than in conventional single shaft irrespective of the welding speed. Jaina et al. [22] carried out numerical simulation analysis of FSW of double stirrer head and found that the peak FSW of double stirrer head temperature is 10 percent higher and minimum temperature is 72 percent higher than conventional FSW and the temperature distribution of double blade is more uniform in thickness and transverse direction.

This new tool designed in this paper has many advantages and some shortcomings. The DRS-FSW has similar advantages as the dual knife FSW in that the combined forces are cancelled for the two opposite directions. Based on the results of the dual knife FSW, it was deduced that the DRS-FSW is also capable of reducing the torque value. Since DRS-FSW is needle-less shoulder and different in size, the working load and tooling requirements of the equipment are lower than that of dual knife FSW. However, the material flow and heat generation of DRS-FSW will be lower than that of dual knife FSW. This paper is a further exploratory study of the dual stirring head technology.

2 Experimental Procedures

This paper presents the use of an independently designed double rotating shoulder friction stir welding device (DRS-FSW) for experiments, as depicted in Fig. 1. The device comprises two shafts of different sizes, a 20-mm diameter stirring head (with a pin root diameter of 6 mm, top diameter of 4 mm, and length of 2.7 mm), and an 8 mm needle-less shoulder. The needle-less shoulder is located on the front side of the stirring head, as illustrated in Fig. 1a and b. The centre distance between the stirring head and the needleless shoulder was 30 mm, where the height difference between the needleless shoulder and the stirring head was 0.1 mm, and the stirring head and the needleless shoulder were rotated in opposite directions. At the centre of the base metal and 1 mm away from the weld seam, a type *K* thermocouple device was installed to record the actual welding temperature, as shown in Fig. 1c. Conventional friction stir welding device is shown in Fig. 1d.

Figure 2 shows the sample preparation method for microstructural characterization and performance testing of the styles. The sample preparation method for microstructural characterization and performance testing of DRS-FSW and FSW is shown in Fig. 2a and b.

The experimental material is AA6061 aluminium alloy with the specification of 150 mm × 100 mm × 3 mm and

its chemical composition is shown in Table 1 [23]. The experimental parameters are shown in Table 2.

3 Simulation Details

The model size was set to be 150 mm × 100 mm × 3 mm and the material was AA 6061 aluminium alloy, and the

Fig. 1 Experimental configuration: **a** schematic view, **b** tool set-up photo, **c** schematics of DRS-FSW, **d** FSW equipment

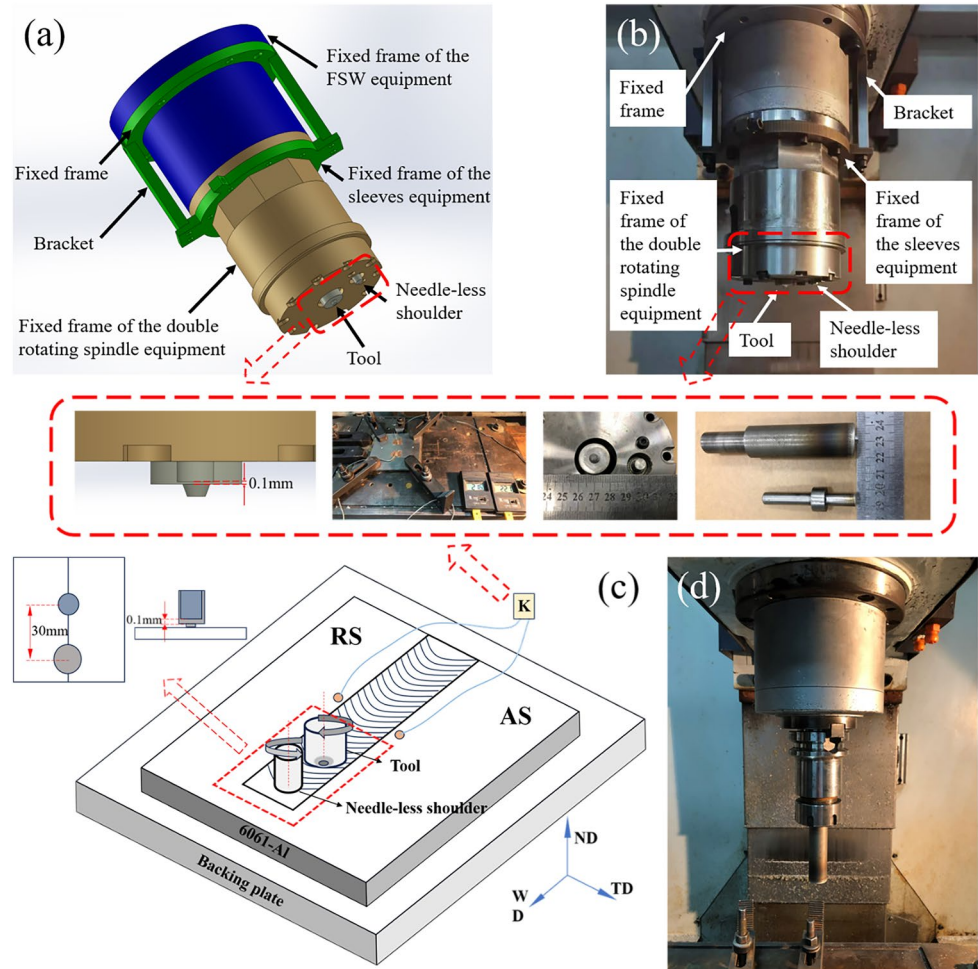


Fig. 2 Sample preparation methods for microstructural characterization and properties testing: **a** DRS-FSW, **b** FSW

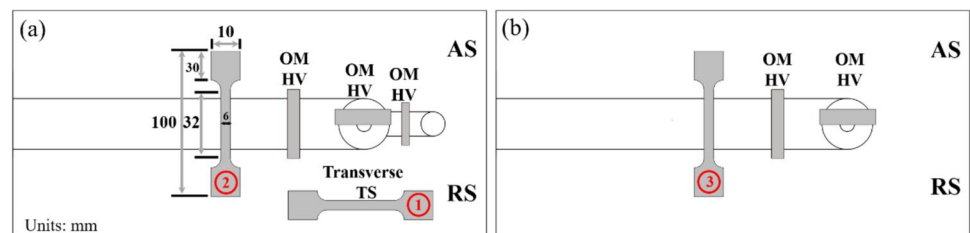


Table 1 Chemical composition of AA 6061 aluminium alloy (mass fraction, %) [23]

Si	Fe	Cu	Mn	Mg	Zn	Ti	Al
0.4–0.8	0.7	0.15–0.40	0.15	0.8–1.2	0.25	0.15	Bal

Table 2 Welding parameters

	Speed (mm/min)	Rotation speed (r/min)	Plunging (mm)	Tilt (°)
Plunging	1	600	0.2	2.5
Welding	30	600	–	2.5

plate, stirring head and needle-less shoulder models were divided into a tetrahedral mesh. As shown in Fig. 3, the needle-less shoulder is set as a rigid body with a mesh number of 10,340 and a node number of 2370; the stirring head is set as a rigid body with a mesh number of 12,285 and a node number of 2792; and the plate is set as a plastic body with a mesh number of 43,488 and a node number of 10,574. Figure 3a and b shows the stirring head, needle-less shoulder and plate position of DRS-FSW and FSW, respectively. Throughout the calculation process, DEFORM-3D automatic mesh reclassification is used, the reclassification criterion is based on whether the depth of mutual penetration between the nodes exceeds the set value, which is set to be 0.7, and the mesh is reclassified to replace the old mesh with the new mesh when the value exceeds 0.7 in the actual calculation process.

Fig. 3 Meshed assembly: a DRS-FSW, b FSW

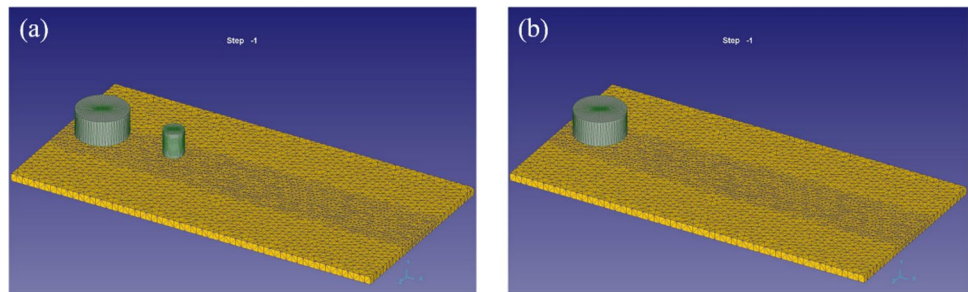


Table 3 Mechanical properties of the workpiece and tool material and heat transfer coefficients [22]

Properties	AA 6061	Tool steel H13
Young’s modulus (MPa)	68,900	210,290
Poisson’s ratio	0.33	0.3
Thermal conductivity (N/s °C)	$f(T)$	24.5
Heat capacity (N/mm ² °C)	$f(T)$	2.78
Heat transfer between workpiece/tool and environment (h_a) (N/mm s °C)	0.02	
Heat transfer between workpiece and tool (N/mm s °C)	11	
Emissivity	0.05	0.7

Table 4 Temperature dependent thermal properties of AA 6061 [22]

Temperature (°C)	37.8	93.3	148.9	204.4	260	315.6	371.1	426.7
Thermal conductivity	162	177	184	192	201	207	217	223
Heat capacity	2.55	2.64	2.71	2.77	2.84	2.91	2.98	3.05

3.1 Material Properties and Calculation Parameters

Table 3 shows the physical parameters of the AA 6061 aluminium alloy and tool steel H13, and Table 4 shows the temperature-dependent thermal properties of the AA 6061 aluminium alloy.

The plate is a rigid visco-plastic material made of AA 6061 aluminium alloy. At high temperatures during plastic deformation, the relationship between rheological stress, rheological rate, and temperature follows a hyperbolic sine function. Therefore, the Arrhenius eigenstructure equation is used to represent it:

$$\dot{\epsilon} = A [\sinh(\alpha\bar{\sigma})]^n \exp\left(-\frac{\Delta H}{RT}\right) \tag{1}$$

where $\dot{\epsilon}$, $\bar{\sigma}$, ΔH , R , T are strain-rate, effective flow stress, activation energy, gas constant and temperature, respectively. A , α and n are the material constants. The Arrhenius model parameters for AA 6061 aluminium alloy are shown in Table 5.

3.2 Simulation Program

In order to simplify the simulation, the following assumptions are made: 1. the workpiece is regarded as a

Table 5 Arrhenius model parameters for AA 6061 aluminium alloy [22]

ΔH (J/mol)	$\ln A$ (s^{-1})	n	α (MPa^{-1})	R (J/mol $^{\circ}C$)
158,300	24.67	5.66	0.045	8.314

continuum and the material model is a rigid-viscoplastic model; 2. the friction and wear of the stirring head and the needle-less shoulder are ignored; 3. the stirring head and the needle-less shoulder are defined as a rigid model; 4. the environmental temperature is set to 20 $^{\circ}C$; 5. the workpiece is fixed, and the velocities of the workpiece are set to zero in the x , y , and z directions; and 6. the default is no tilt angle.

The simulation of DRS-FSW is divided into two steps: the plunging stage and the welding stage. The chosen behavior is shear friction:

$$f = mk$$

where f and k are contact shear stress and yield shear stress of the material, respectively. m is the shear factor which is defined as 0.4 based on the calibration carried out by the authors [22].

4 Results and Discussion

4.1 Temperature Field Simulation Analysis

Figure 4 shows the surface and profile temperature field distributions of the workpieces of DRS-FSW and FSW at a downward pressing speed of 1 mm/min and a rotational speed of 600 r/min. At the end of the plunging stage, DRS-FSW reaches a maximum temperature of 503 $^{\circ}C$. The temperature range in the needle-less shoulder region lay between 262 and 323 $^{\circ}C$, and the temperature at the center is 280 $^{\circ}C$. The cloud map of the temperature distribution shows an ‘umbrella’ shape (red dotted line), as shown in Fig. 4a. FSW has a maximum temperature of 495 $^{\circ}C$ at the end of the Plunging stage, the position of the same point as DRS-FSW has a temperature of 140 $^{\circ}C$, cloud map of temperature distribution showing “concentric circles” shape, as shown in Fig. 4b. The profiles indicate that DRS-FSW has wider temperature-affected zones and higher temperatures than FSW. DRS-FSW and FSW show a different temperature field in the downward pressing stage. DRS-FSW has an assisted heat generation from the front shoulder, so the metal to be welded on the front side has a higher temperature and a larger high-temperature region. The highest temperatures of DRS-FSW and FSW are found in the

shoulder edge zone, because the frictional heat generated by the stirring head’s shoulder and the workpiece is the main heat source of FSW during the welding process [24].

Figure 5 shows the surface and profile temperature field distribution of the workpieces of DRS-FSW and FSW at a welding speed of 30 mm/min and a rotation speed of 600 r/min. At the welding stage, DRS-FSW reaches a maximum temperature of 568 $^{\circ}C$. The temperature range in the needle-less shoulder region lay between 366 to 399 $^{\circ}C$, and the temperature at the center is 388 $^{\circ}C$, as shown in Fig. 5a. FSW has a maximum temperature of 521 $^{\circ}C$ at the welding stage, the position of the same point as DRS-FSW has a temperature of 353 $^{\circ}C$, temperatures in this region range from 347 to 376 $^{\circ}C$, as shown in Fig. 5b. The longer the welding time between DRS-FSW and FSW, the more similar the temperature ranges become, as shown in the temperature cloud map distribution (surface and profile). During the welding stage, the needle-less shoulder of the DRS-FSW preheats the area to be welded. However, due to its size, there is a ceiling to the amount of heat it can produce. Over time, the heat production of the stirring head exceeds that of the needleless shoulder. As a result, the temperature ranges of DRS-FSW and FSW become increasingly similar in the later stages of the weld.

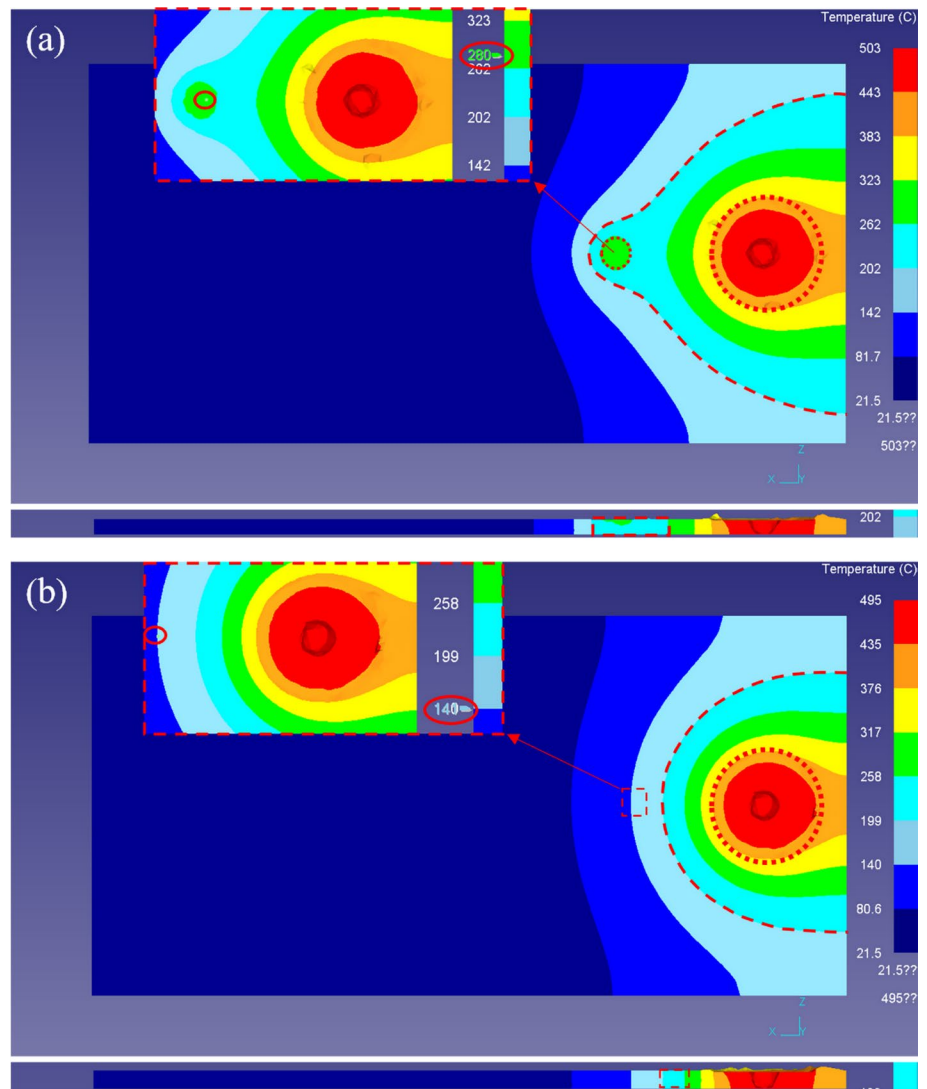
As shown in Fig. 6, based on the temperature simulation results of the DRS-FSW and FSW plunging stage and welding stage, the temperature changes have been summarised along the y -axis for both processes to better display the variation. Temperature was measured at three lines along the y -direction on the front side of the stirring head, specifically at the center of the weld ($x = 0$ mm), the right side of the weld ($x = 5$ mm), and the left side of the weld ($x = -5$ mm). Figure 6a–d depicts the plunging and welding stages of both DRS-FSW and FSW. Figure 6e displays the temperature distribution of DRS-FSW and FSW Plunging stage. It is evident that the temperature of DRS-FSW is higher than that of FSW at 1–10 mm. However, the temperatures of both converge at 11–16 mm. Figure 6f shows the temperature distribution of DRS-FSW and FSW welding stage. At this point, the temperature difference between the two is around 15 $^{\circ}C$, and the difference in temperature change is rather small.

Based on the simulation results, it can be concluded that DRS-FSW has a higher temperature than FSW during the plunging stage. However, as the welding time passes, the temperature ranges of the two become closer.

4.2 Strain Field and Material Flow Analysis

Figure 7 shows the strain field distribution characteristics of the DRS-FSW and FSW weld zone. As shown in Fig. 7a, the strain in the DRS-FSW weld zone is mainly concentrated

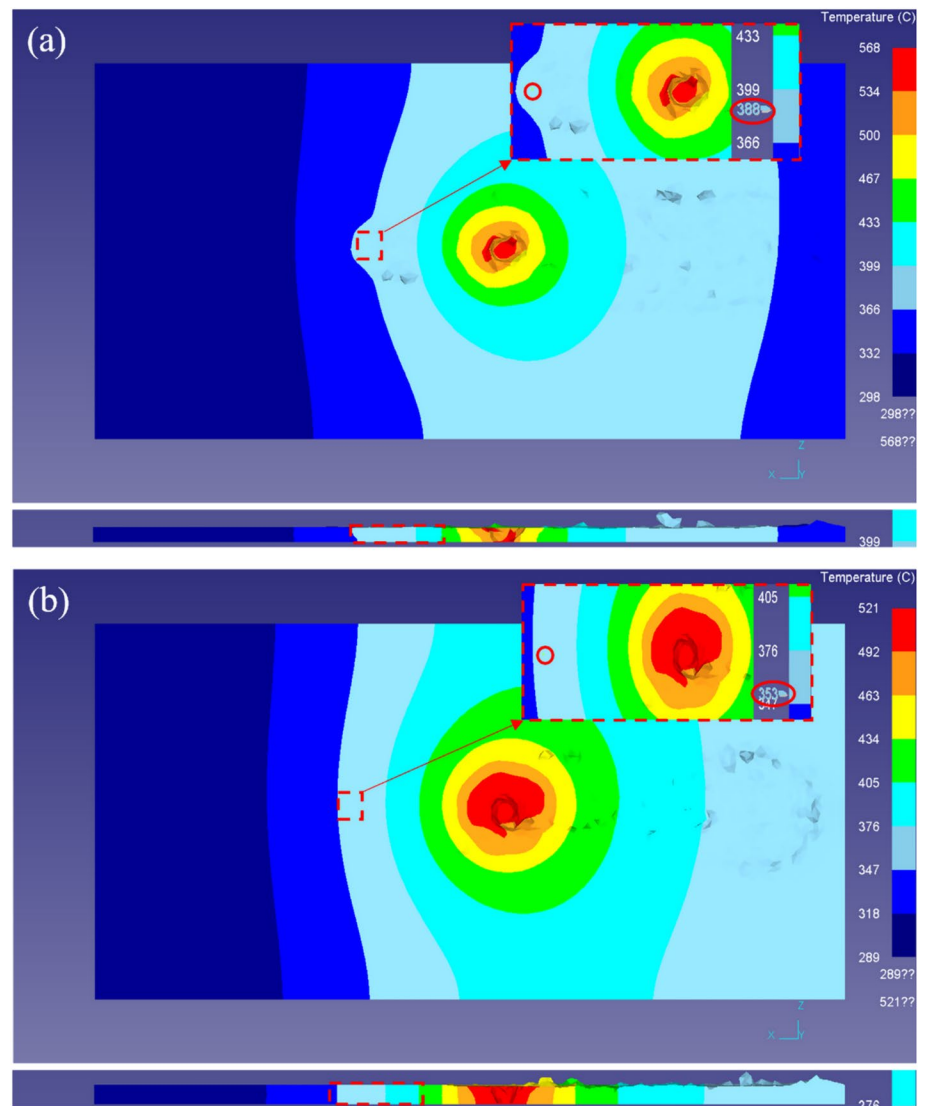
Fig. 4 Temperature field during the plunging stage: **a** DRS-FSW, **b** FSW (color figure online)



at the stirring head, and the colour depth of the lower part of the stirring head is higher than that of the upper part in the planar strain cloud, and the cross-sectional strain distribution in the weld zone shows an asymmetric distribution along the stirring needle, and in the transverse direction, it shows that the strain on the advancing side (AS), where the stirring needle's rotational direction is consistent with the welding direction, is higher than that on the retarding side (RS), where the rotational direction is opposite to the welding direction. Retreating side, where the direction of rotation is opposite to the welding direction, and the strain distribution on the weld surface in the weld zone is mainly characterised by the strain occurring in the middle of the needleless shoulder and the stirring head. Figure 7b shows that the cross-section strain distribution in the weld zone of FSW is the same as that of DRS-FSW, and the strain distributions in the plane and weld surface are not the same as that of DRS-FSW.

As shown in Fig. 8, two columns of tracer points were set up at the front side of the shoulder to analyse the difference in material flow between the DRS-FSW and FSW weld zones through the displacement of the tracer points after welding. As shown in Fig. 8a, after the needleless shoulder travelled, the tracer points at the middle were displaced downwards, followed by a large displacement around the rotational direction of the stirring head, which showed a discrete distribution of AS and RS tracer points after leaving the stirring head's action area, and a dense distribution of tracer points at the centre of the weld. As shown in Fig. 8b, most of the tracer points moved around the rotational direction of the stirring head, and the positions of the tracer points were biased from AS to RS after leaving the stirring head's action zone, which is the material flow behaviour of a typical conventional FSW.

Fig. 5 Temperature field during the welding stage: **a** DRS-FSW, **b** FSW



4.3 Joint Morphology and Temperature Analysis

Figure 9 shows the surface formation of the welded joint between DRS-FSW and FSW at a rotational speed of 600 r/min and a welding speed of 30 mm/min. It can be seen that under the welding parameters, the stirring head and the metal undergo intense stirring and friction, the weld metal is completely plasticised and with the stirring head together with a good plastic flow, and ultimately lead to the formation of a smooth surface and grain tight defect-free weld. The surface morphology of DRS-FSW is shown in Fig. 9a and FSW in Fig. 9b.

Figure 10 shows the macroscopic morphology of welded joints for DRS-FSW and FSW at a rotational speed of 600 r/min and welding speed of 30 mm/min. As shown in Fig. 10a and d, the macroscopic morphology of the joint cross section of both is “bowl-shaped”, and the upper surface of the weld is wider than the lower

surface, in which the distributions of the stirred zone (SZ), thermo-machine-affected zone (TMAZ), heat-affected zone (HAZ), and base material zone (BM) of the joint are basically the same. However, the area below the shoulder on the advancing side (AS) shows different morphological characteristics, and the DRS-FSW has a wider and deeper morphology at this location than that of the FSW, indicating that the 8-mm needle-less shoulder affects the macroscopic morphology of the welded joints. Figure 10b and e shows the macroscopic morphology of the longitudinal cross section of the welded joint, the difference between the two being the mixing zone of the stirring head and the needle-less shoulder (Fig. 10b mini-plot). The size and morphology of the grains in the mixing zone were elongated along the direction of the maximum shear stress, so that the grain morphology at the edges of the zone of influence of the mixing head and the zone of influence of the needle-less shoulder showed two directions. The grains

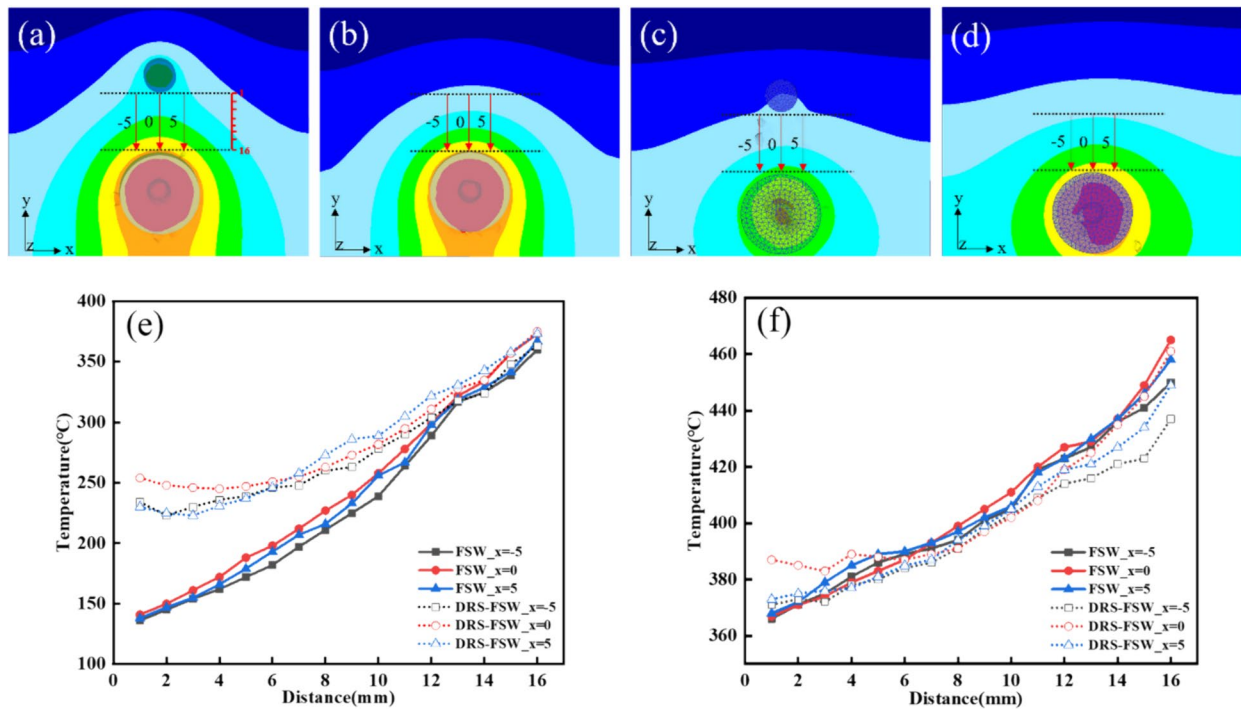


Fig. 6 Temperature change in y-direction: **a** DRS-FSW during the plunging stage, **b** FSW during the plunging stage, **c** DRS-FSW during the welding stage, **d** FSW during the welding stage, **e** Temperature change during plunging stage, **f** Temperature change during welding stage

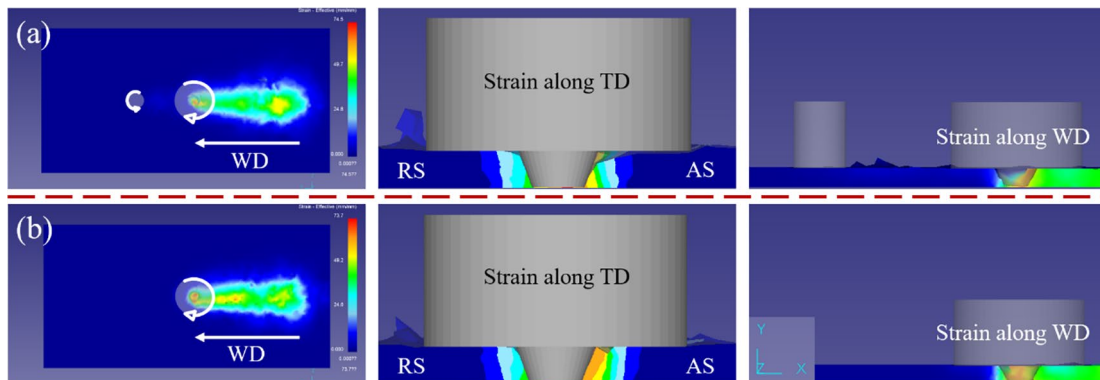


Fig. 7 Characteristics of strain distribution in the weld zone: **a** Plastic strain in the weld zone of DRS-FSW, **b** Plastic strain in the weld zone of FSW

in the middle of the mixing zone showed irregular size and morphology influenced by the front and back axial shoulders, which is similar to the results of the study by Li et al. [25]. Figure 10c shows the cross-sectional macroscopic morphology of the DRS-FSW needle-less shoulder welded joint, which is typical of the macroscopic morphology of friction stir welded joints.

Figure 11 shows the actual and simulated predicted temperatures for DRS-FSW and FSW. The simulated and actual temperature changes of both methods show a good correlation. The peak temperature predicted by simulation

for DRS-FSW is 448 °C, while the actual peak temperature is 426 °C, as shown in Fig. 11a. For FSW, the simulated predicted peak temperature is 428 °C, while the actual peak temperature is 415 °C, as shown in Fig. 11b. The experimental results show that the preheating effect of the DRS-FSW process is evident in the early stages of the welding process, validating the results obtained from the preliminary simulations. The model accurately predicts temperature variations during welding in the DRS-FSW process, as demonstrated by data from simulations and experiments.

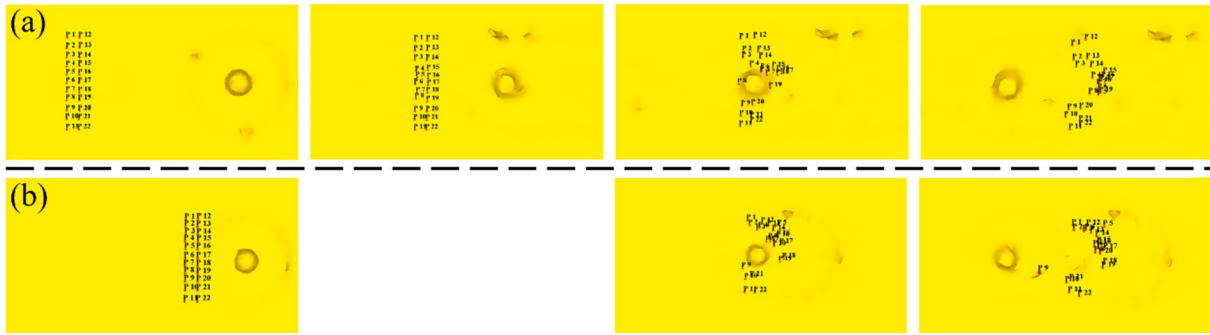


Fig. 8 Characteristics of material flow distribution in the weld zone: **a** material flow in the weld zone of DRS-FSW, **b** Plastic strain in the weld zone of FSW

Fig. 9 Surface morphology of welded joints: **a** DRS-FSW, **b** FSW

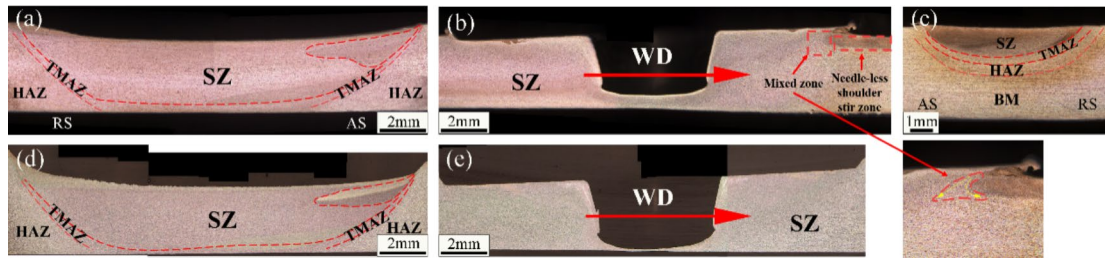
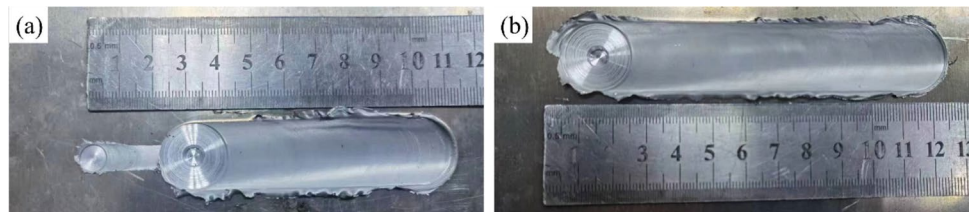
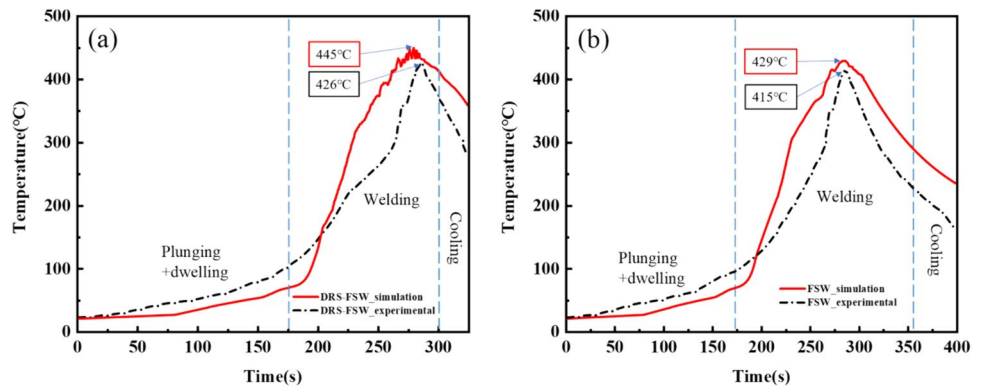


Fig. 10 Macroscopic morphology of welded joints: **a** DRS-FSW cross section, **b** DRS-FSW longitudinal section, **c** Needle-less shoulder, **d** FSW cross section, **e** FSW longitudinal section

Fig. 11 Comparison of simulation predicted temperature with experiment: **a** DRS-FSW, **b** FSW



4.4 Mechanical Properties

Figure 12 shows the microhardness distribution characteristics of the welded joint cross section and different thickness

positions of DRS-FSW and FSW. The microhardness measurement dimensions are the same as the weld dimensions; therefore, it does not exhibit a typical ‘W’-shaped distribution. The cross-sectional hardness curves of the welded

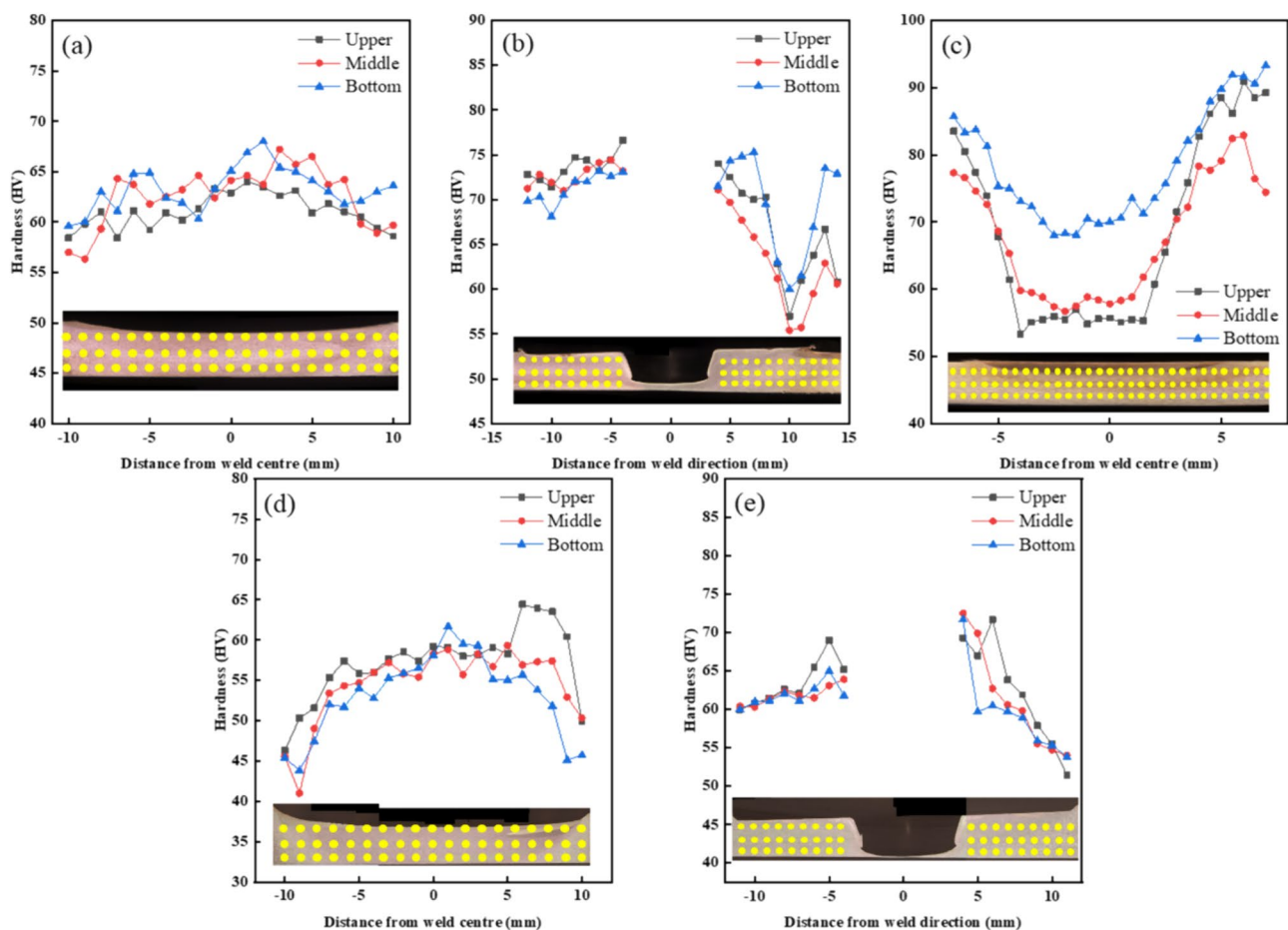


Fig. 12 Joint microhardness distribution: **a** DRS-FSW cross section, **b** DRS-FSW longitudinal section, **c** Needle-less shoulder, **d** FSW cross section, **e** FSW longitudinal section

joints of the two illustrate that the stirred zone (SZ) has the highest microhardness and the distribution of hardness along the thickness direction varies less, as shown in Fig. 12a and d. The longitudinal cross-section hardness curves of the two welded joints illustrate that the microhardness in the stirred zone is higher than that in the unstirred zone and is uniformly distributed along the thickness direction, as shown in Fig. 12b and e. The cross-sectional microhardness profile of the DRS-FSW needle-less shoulder welded joints illustrates that the highest microhardness is observed in the base material on both sides, with lower hardness in HAZ and TMAZ, and increased hardness in SZ, and the joints showed differences in the microhardness along the thickness direction, with lower hardness in the upper and intermediate layers, and the highest hardness in the bottom layer, as shown in Fig. 12c. It was analysed that the high hardness of SZ is a result of welding thermal cycles at higher

temperatures and intense plastic deformation, which leads to fine recrystallized grains in the region [26]. In contrast, HAZ is only subjected to thermal cycling, resulting in grain growth and lower microhardness values [27]. TMAZ has undergone partial dynamic recrystallization due to thermal action and forces, resulting in a hardness level between that of SZ and HAZ [28].

Figure 13 shows the engineering stress–strain curves for DRS-FSW and FSW joints. The tensile test results in the figure indicate that the base metal (BM) sample has fractured from the center position with a tensile strength of 276 MPa. The DRS-FSW and FSW samples have fractured at the neck position on the advancing side (AS) and retreating side (RS), respectively, with tensile strengths of 260 MPa and 264 MPa. Both samples have fractured in the vicinity of the base metal region, demonstrating good weldability. Figure 14 shows different magnification SEM morphology of

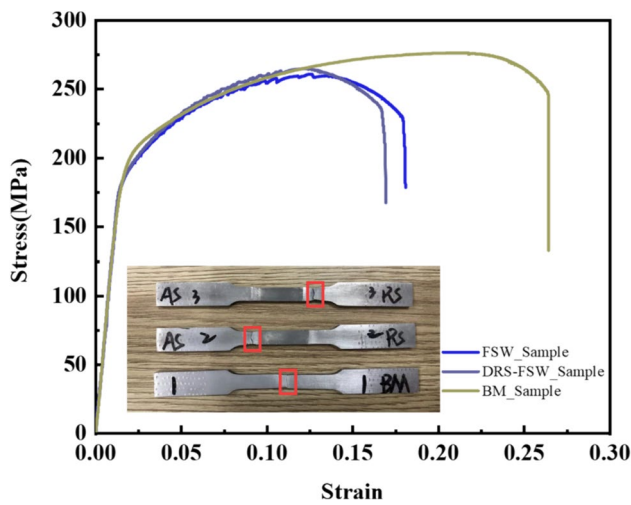


Fig. 13 DRS-FSW tensile test results

BM, DRS-FSW and FSW joint fracture. Figure 14a–c shows that the tensile fracture of all three samples exhibits large equiaxial toughness dimples and tearing ribs, indicating good plasticity and toughness characteristics. Figure 14d–f reveals that the stripping of tiny second-term particles leave behind small, smooth, tough dimples on the fracture surface at high magnification. Additionally, microcracks are observed on the grain boundaries. Larger tough dimples contain coarse second-phase particles that are caused through crystal fracture [29].

5 Conclusions

This paper compares the properties of DRS-FSW and FSW on AA 6061 FSW joints at a rotational speed of 600 r/min and a welding speed of 30 mm/min using a combination of simulation and experiment. The following conclusions can be drawn:

- (1) The simulation results for the plunging stage of DRS-FSW using FSW show that the temperature in the needle-less shoulder area reaches 280 °C, which is significantly higher than the corresponding temperature in FSW. The temperature profile indicates that DRS-FSW has a wider and higher temperature distribution. The simulation results of the welding stage for DRS-FSW and FSW show that as the welding time progresses, the temperature intervals for DRS-FSW and FSW become increasingly similar later in the welding process.
- (2) The experimental results of DRS-FSW and FSW show differences in the macroscopic morphology of the joints. The temperature profile also indicates that DRS-FSW has a preheating effect in the pre-welding stage, which decreases over time. The model accurately predicts the temperature changes during the working of the DRS-FSW.
- (3) The hardness distributions of DRS-FSW and FSW joints are similar, with tensile strengths of 260 MPa and 264 MPa, respectively. The fracture morphology exhibits numerous tough dimples, indicating good plasticity of the joints.

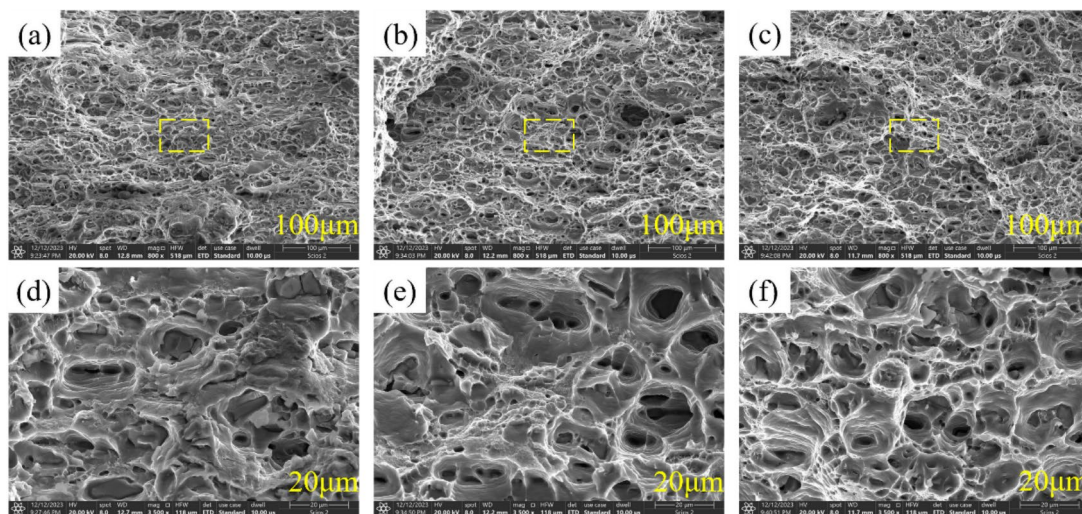


Fig. 14 Joint fracture SEM morphology: a–c BM, DRS-FSW, FSW sample low-power morphology, d–f BM, DRS-FSW, FSW sample of high-power morphology

Acknowledgements All authors were involved in the study conceptualization and design, all commented on previous versions of the manuscript, and all authors read and approved the final manuscript. Tao Sun contributed to methodology, investigation and reviewing; Zhenkui liang helped in sample testing; Yongqi Yang helped in reviewing and editing; Xiaomei Feng done resources and editing; Yifu Shen helped in funding acquisition, resources and supervision.

References

1. Thomas W M, Nicholas E D, Needham J C, Murch M G, Temple-Smith P, and Dawes C J, International patent number PCT/GB92/02203 and GB patent application number 9125978.9 (1991)
2. Mishra R S, and Ma Z Y, *Mat Sci Eng R* **50** (2005) 1. <https://doi.org/10.1016/j.mser.2005.07.001>
3. Kayode O, and Akinlabi E T, *Mater Res Express* **6** (2019) 112005. <https://doi.org/10.1088/2053-1591/ab3262>
4. Cao F, Huang G, Hou W, Ni R, Sun T, Hu J, Shen Y, and Gerlich A P, *J Mater Process Technol* **307** (2022) 117660. <https://doi.org/10.1016/j.jmatprotec.2022.117660>
5. Cao F, Sun T, Hu J, Hou W, Huang G, Shen Y, Ma N, Geng P, Hu W, and Qu X, *Mater Des* **225** (2023) 111492. <https://doi.org/10.1016/j.matdes.2022.111492>
6. Fei X, Jin X, Ye Y, Xiu T, and Yang H, *Mater Sci Eng A* **653** (2016) 43. <https://doi.org/10.1016/j.msea.2015.11.101>
7. Yaduwanshi D K, Bag S, and Pal S, *Mater Des* **92** (2016) 166. <https://doi.org/10.1016/j.matdes.2015.12.039>
8. Kaushik P, and Dwivedi D K, *Mater Today* **46** (2021) 1091. <https://doi.org/10.1016/j.matpr.2021.01.438>
9. Li J Q, and Liu H J, *Int J Adv Manuf Technol* **66** (2013) 623. <https://doi.org/10.1007/s00170-012-4353-3>
10. Widener C A, Talia J E, Tweedy B M, and Burford D A, *High-rotational speed friction stir welding with a fixed shoulder*, Proceedings of the 6th International Symposium on Friction Stir Welding, Montreal (2006)
11. Li J Q, and Liu H J, *Mater Des* **43** (2013) 299. <https://doi.org/10.1016/j.matdes.2012.07.011>
12. Li J Q, Liu H J, and Duan W J, *Int J Adv Manuf Tech* **64** (2013) 1685. <https://doi.org/10.1007/s00170-012-4132-1>
13. Barbini A, Carstensen J, and dos Santos J F, *J Mater Sci Technol* **34** (2018) 119. <https://doi.org/10.1016/j.mst.2017.10.017>
14. Sinhmar S, and Dwivedi D K, *J Mater Process Technol* **277** (2020) 116482. <https://doi.org/10.1016/j.jmatprotec.2019.116482>
15. Saravana Sundar A, Kar A, Mugada K K, and Kumar A, *Mater Charact* **203** (2023) 113148. <https://doi.org/10.1016/j.matchar.2023.113148>
16. Thomas W M, Threadgill P L, and Nicholas E D, *Sci Technol Weld Join* **4** (1999) 365.
17. Mitsuo H, Friction agitation joining method and Frictional Agitation joining device' Patent Abstracts of Japan, Publication number 2000-094156, Date of publication of application 04.04.2000
18. Thomas W M, Braithwaite A B M, and John R, *Skew-Stir™ Technology*, Proceedings of the 3rd International Symposium on Friction Stir Welding, Port Island, Japan (2001)
19. Thomas W M, Norris I M, Smith I J, and Staines D G, *Reversal stir welding—Re-stir™—feasibility study*, Proceedings of the 4th International Symposium on Friction Stir Welding, Park City, Utah, USA (2003)
20. Thomas W M, Norris I M, Staines D G, and Watts E R, *Friction stir welding—process Developments and Variant Techniques*, The SME Summit, Oconomowoc, Milwaukee, WI (2005)
21. Kumari K, Pal S K, and Singh S B, *J Mater Process Technol* **215** (2015) 132. <https://doi.org/10.1016/j.jmatprotec.2014.07.031>
22. Jaina R, Kumari K, Pal S K, and Singh S B, *J Mater Process Technol* **255** (2018) 121. <https://doi.org/10.1016/j.jmatprotec.2017.11.043>
23. Zhao P-F, Ren G-S, Guang-Sheng, Xu C-G, and Shen Z, *J Plast Eng* **04** (2006) 79.
24. Zhang Y, Cao X, Larose S, and Wanjara P, *Can Metall Q* **51** (2012) 250.
25. Li J Q, and Liu H J, *J Mater Sci Technol* **31** (2015) 375e383. <https://doi.org/10.1016/j.jmst.2014.07.020>
26. Kwang-Jin L, and Eui-Pyo K, *Trans Nonferrous Met Soc China* **24** (2014) 2374. [https://doi.org/10.1016/S1003-6326\(14\)63359-8](https://doi.org/10.1016/S1003-6326(14)63359-8)
27. Moreira P M G P, Santos T, Tavares S M O, Richter-Trummer V, Vilaça P, and de Castro P M S T, *Mater Des* **30** (2009) 180. <https://doi.org/10.1016/j.matdes.2008.04.042>
28. Jamshidi Aval H, Serajzadeh S, and Kokabi A H, *Mater Sci Eng A* **528** (2011) 8071. <https://doi.org/10.1016/j.msea.2011.07.056>
29. Chen Y, Hu H, Huang C, *Friction stir welding technology*, CHINA MACHINE PRESS, May 2018, (2018), p 62, Paperback ISBN: 9787111595458, <https://www.cmpbook.com>

Publisher's Note Springer Nature remains neutral with regard to jurisdictional claims in published maps and institutional affiliations.

Springer Nature or its licensor (e.g. a society or other partner) holds exclusive rights to this article under a publishing agreement with the author(s) or other rightsholder(s); author self-archiving of the accepted manuscript version of this article is solely governed by the terms of such publishing agreement and applicable law.